Scandium and aluminum substitution and energy transfer processes in the undoped and Ce-doped $Y_3Sc_xAl_{5-x}O_{12}$ scintillation crystals

V. Laguta [1,*] J. Pejchal [1] V. Babin [1] A. Beitlerova,[1] Yu. Zagorodniy [2] J. Jezek [1,3]
D. Sedmidubsky [3] A. Resetic [4] and M. Nikl [1]

[1] *Institute of Physics of the Czech Academy of Sciences, Cukrovarnicka 10/112, Prague 16200, Czech Republic*
[2] *Frantsevich Institute for Problems in Materials Science, National Academy of Sciences of Ukraine, 3, str. Omeliana Pritsaka, 03142 Kyiv, Ukraine*
[3] *Department of Inorganic Chemistry, University of Chemistry and Technology, Technická 5, Prague 166 28, Czech Republic*
[4] *Jozef Stefan Institute of Slovenia, Jamova 39, 1000 Ljubljana, Slovenia*

(Received 18 December 2025; accepted 24 March 2026; published 17 April 2026)

The structural and scintillation properties of pure and Ce-doped $Y_3Sc_xAl_{5-x}O_{12}$ ($x = 0$, 0.05, 1.16, and 2) crystals were systematically investigated. High-resolution ^{45}Sc and ^{27}Al magic angle spinning nuclear magnetic resonance spectroscopy revealed that Sc^{3+} ions predominantly occupy octahedral sites, effectively replacing Al^{3+} ions, while antisite Sc at Y dodecahedral positions remains below 0.2 at.%. Sc incorporation into $Y_3Al_5O_{12}$ induces strong exciton emission at 320–324 nm, nearly 10 times higher than that of reference $Bi_4Ge_3O_{12}$ (BGO) crystal, even at low Sc concentrations (5 at.%). Ce^{3+} doping introduces characteristic $5d^1 \rightarrow 4f$ emission at 518 nm, accelerates scintillation decay, and in combination with Mg^{2+} codoping, promotes the formation of Ce^{4+} ions that enable a fast radiative de-excitation pathway. $Y_3Sc_2Al_3O_{12}$: Ce exhibits a maximum scintillation light yield of 80–84% relative to BGO with a mean decay time of 85–110 ns. Thermostimulated liminescence and electron paramagnetic resonance studies indicate that holes are mainly trapped at oxygen ions near Sc ions (O^- centers), while electrons are primarily localized at Sc antisite ions near oxygen vacancies (Sc^{2+}–V_O centers), affecting scintillation kinetics. Density functional theory calculations confirm that Sc^{3+} at the dodecahedral site forms a deep electron trap. These results highlight the key role of Sc and Ce in tuning emission, decay dynamics, and defect-mediated processes in Sc-admixed multicomponent garnet scintillators.

DOI: 10.1103/png3-xnt7

I. INTRODUCTION

The discovery of multicomponent garnet single crystal scintillators [1] marked the beginning of a new era in the research and development of oxide scintillators. Through band-gap engineering, $Gd_3Al_{5-x}Ga_xO_{12}$:Ce (GAGG:Ce), with $2 < x \leqslant 3$, emerged as the most efficient bulk oxide single-crystal scintillator, offering additional practical advantages such as mechanical and chemical stability and reliable large-scale crystal growth [2]. Their preparation, luminescence, and scintillation properties as a function of chemical composition as well as energy transfer processes, charge-trap behavior, and the role of traps in the scintillation mechanism have been extensively investigated in laboratories worldwide [3–16].

Another important achievement was reported: the suppression of slow components in the scintillation response of the Ce-doped garnets. This improvement resulted from the stabilization of Ce^{4+}, which provides an additional fast radiative de-excitation pathway and competes with the undesirable capture of migrating electrons in traps [17,18]. Stabilization and increased concentration of Ce^{4+} centers are achieved through codoping with divalent ions (Mg^{2+}, Ca^{2+}), following a strategy previously successful in Ce-doped $(LuY)_2SiO_5$ orthosilicates [19]. The effect of such divalent-ion codoping in multicomponent garnets has been studied further [20–23], and significant acceleration of the scintillation response in heavily doped materials has recently been reported and attributed to luminescence quenching in closely spaced Ce–Mg pairs [24,25]. This finding is highly promising for applications in ultrafast scintillation detectors used in accelerators and advanced instrumentation.

Due to gallium in the chemical formula, crystal growth from the melt requires the use of iridium crucibles [26], which makes the production very costly. This raises an important question: Can the electronic band structure of such multicomponent garnets be engineered—and electronic traps suppressed—in a manner similar to GAGG:Ce but using a chemical composition that allows growth with a cheaper technology, such as molybdenum crucibles commonly used in the industrial production of $Y_3Al_5O_{12}$:Ce (YAG:Ce) or $Lu_3Al_5O_{12}$:Ce (LuAG:Ce) single crystals [27]?

A promising candidate is the family of Sc-admixed garnets with the general formula $(Gd)_3(Al, Sc)_2Al_3O_{12}$ [often written as $Gd_3(Sc, Al)_5O_{12}$], doped with Ce^{3+} (GSAG:Ce). These

*Contact author: laguta@fzu.cz

materials have recently been revisited in the literature [28,29], and their successful growth in molybdenum crucibles has been confirmed. The presence of Sc shifts the bottom of the conduction band downward, like Ga in the Ga-admixed garnets [30], and melt growth behavior has also been investigated [31,32].

These Ce-doped Gd–Sc–Al multicomponent garnets, however, exhibit a significantly lower light yield of about 10 000 ph/MeV [29,32] compared with standard GAGG:Ce. A very recent study aimed at optimizing GSAG:Ce grown by the micropulling-down (micro-PD) technique [33] achieved a notably higher light yield of around 17 000 ph/MeV, yet this value remains more than a factor of two lower than that of GAGG:Ce grown by the same method, which reaches approximately 40 000 ph/MeV, consistent with previous reports [1]. The deterioration in scintillation performance has been attributed to deep electron traps associated with Sc occupying the dodecahedral site of the garnet structure, a hypothesis supported by theoretical calculations of the electronic band structure [33].

However, the actual site occupancy of Sc ions in the GAGG:Ce solid solution remains insufficiently understood. In this context, nuclear magnetic resonance (NMR) of both Sc and Al nuclei could, in principle, provide insight into Sc-to-Al distributions, as previously demonstrated for Ga and Al site occupancy among octahedral and tetrahedral positions in $Y(Lu)_3Ga_xAl_{5-x}O_{12}$ solid solutions [7,34]. Unfortunately, detailed studies of lattice-site occupation by Sc using NMR—as well as investigations of charge traps by electron paramagnetic resonance (EPR)—are hindered in Gd-containing garnets. The presence of paramagnetic Gd^{3+} ions leads to severe spectral broadening, rendering both NMR and EPR spectra essentially uninformative.

The purpose of the present paper is to elucidate the lattice-site occupancy of Sc^{3+} and Al^{3+} ions in Gd-free $Y_3(Sc, Al)_5O_{12}$ garnet crystals grown by the micro-PD method and to investigate their role in energy-transfer and charge-capture processes, which allow for the combined use of magnetic resonance and optical spectroscopies. In particular, Sc-to-Al ordering within the $Y_3(Sc, Al)_5O_{12}$ garnet lattice was studied using ^{45}Sc and ^{27}Al magic angle spinning (MAS) NMR. Ce^{3+} site occupancy and its conversion to Ce^{4+} were examined via Ce^{3+} EPR, which also provides detailed insight into charge-carrier transfer and trapping within the lattice. The study is complemented by theoretical calculation of electronic band structure and measurements of selected optical, luminescence, and scintillation properties of both Ce-free and Ce-doped $Y_3(Sc, Al)_5O_{12}$ crystals.

II. EXPERIMENTAL DETAILS

Three types of crystals were measured: (i) $Y_3Al_5O_{12}$ slightly doped with 5 at.% Sc, grown by the Czochralski method, (ii) congruent composition $Y_{2.89}Sc_{1.16}Al_{3.95}O_{12}$:0.1% Ce crystals codoped with Mg^{2+} ions (0, 300, and 1000 ppm), grown by the micro-PD method [35,36] in Ir crucible under N_2 atmosphere, and (iii) stoichiometric $Y_3Sc_2Al_3O_{12}$, $Y_3Sc_2Al_3O_{12}$:0.1% Ce grown by the micro-PD method in Mo crucible under an Ar + 5% H_2 atmosphere. All the compositions given correspond to the nominal (melt) compositions.

The micro-PD growth was performed using the T-MPD-OX apparatus (Akita Seiko Co., Japan) with radiofrequency inductive heating, from the corresponding mixtures of 4N purity Y_2O_3, Al_2O_3, Sc_2O_3, MgO, and CeO_2 oxides from Shin-Etsu Co., Japan. The Ir or Mo crucibles had a die of 3 mm in diameter and nozzle diameter of 0.5 and 2 mm, respectively. The [111] oriented Czochralski-grown YAG single crystal (provided by Crytur Co. Ltd., Czech Republic) was used as a seed. The crucible was placed on an afterheater with windows and on alumina pedestal. The hot zone around the crucible consisted of three layers of alumina shielding for thermal insulation. The atmosphere gas flow was kept at 0.5 L/min. The crucible with the starting materials was heated up to the melting temperature, which is around 1900 °C. Then the YAG single-crystal seed was brought into contact with the melt coming through the nozzle due to the capillary action. Unlike for the Ga_2O_3 counterpart, no Sc_2O_3 evaporation was observed due to its extremely high melting point above 2400 °C [37], which significantly exceeds the overall melt temperature during the growth.

While the applied technology is well optimized for the growth of Ga- and Sc-admixed single-phase crystals (as confirmed by x-ray diffraction measurements of similar crystals [29,38]), the grown crystals were primarily polycrystalline, with individual crystallites misoriented by no more than 5°. For NMR and some EPR measurements, the crystals were ground into powder, while for optical measurements, small plates (1 mm thick, 3–5 mm in diameter) with both faces polished were used.

Room-temperature MAS ^{45}Sc and ^{27}Al NMR spectra of powder samples were recorded on a Bruker Advance III 500 MHz high-resolution solid-state NMR spectrometer at a spinning rate of 24 kHz in a magnetic field of 11.75 T, corresponding to Larmor frequencies of 121.500 MHz for ^{45}Sc and 130.329 MHz for ^{27}Al. A single-pulse sequence with short $\pi/12$ pulses (0.117 μs for ^{45}Sc and 0.267 μs for ^{27}Al) was employed to achieve uniform excitation of Sc and Al nuclei with different quadrupole coupling constants at various lattice sites. For each sample, 17 000 scans for ^{45}Sc and 800 scans for ^{27}Al were accumulated, with recycle delays of 5 and 80 s, respectively. Spectra were referenced to the Larmor frequency of the observed nuclei. Experimental spectra were analyzed using the Bruker TopSpin software [39] and fitted with the dmfit program [40].

EPR spectra were recorded using a Bruker EMX Plus spectrometer operating at X-band (microwave frequency 9.25–9.5 GHz) over a temperature range of 10–290 K. X-ray irradiation of the crystals was performed using an ISO-DEBYEFLEX 3003 Seifert GmbH X-ray tube with a Co anode, operating at 55 kV and 30 mA.

Absorption spectra were recorded using a Shimadzu 3101PC UV/VIS/NIR spectrophotometer in the range 190–800 nm. Radioluminescence (RL), photoluminescence excitation (PLE), photoluminescence (PL) spectra, and PL decay curves were measured using a custom-built 5000M spectrofluorometer (Horiba Jobin Yvon). Excitation sources included a W x-ray tube (40 kV, 15 mA, Seifert) for RL, a steady-state xenon lamp (EQ-99X LDLS, Energetic, a Hamamatsu Company) for PLE, and nanosecond nanoLED pulsed sources (IBH Scotland) for PL. Fast decay measurements were

performed using time-correlated single-photon counting. The detection system comprised a single-grating monochromator and a TBX-04 photon-counting detector (IBH Scotland). All measured spectra were corrected for spectral detection sensitivity (RL, PL) and excitation energy (PLE). PL and scintillation decay curves were analyzed using a convolution procedure to extract true decay times (SpectraSolve software, Ames Photonics).

For quantitative RL measurements, a $Bi_4Ge_3O_{12}$ (BGO) standard scintillator of similar dimensions was measured under identical experimental conditions. Thermostimulated luminescence (TSL) glow curves were recorded with the 5000M spectrofluorometer over 77–500 K using a Janis cryostat at a heating rate of 0.1 K/s, after excitation with the x-ray tube at 77 K.

The electronic structure calculations and the structural optimizations were based on the density functional theory (DFT) and were performed in MedeA software by the implemented program VASP [41,42]. The methodology of calculations is described in Sec. III C.

III. EXPERIMENTAL RESULTS

A. ^{27}Al and ^{45}Sc NMR in $Y_3Sc_xAl_{5-x}O_{12}$

In the $Y_3Sc_xAl_{5-x}O_{12}$ solid solution, similar to the $Y_3Al_5O_{12}$ garnet lattice, Al^{3+} ions can occupy both tetrahedral sites (surrounded by four oxygen ions) and octahedral sites (surrounded by six oxygen ions). In contrast, due to the larger ionic radius of Sc^{3+} as compared with Al [43], these ions must predominantly occupy larger octahedral positions. Consequently, the presence of Sc also influences the distribution of Al between octahedral and tetrahedral sites. Occupation of other lattice sites, such as tetrahedral or Y dodecahedral positions, by Sc at low concentrations cannot be entirely excluded. Such antisite Sc^{3+} ions can act as effective electron traps under x-ray or γ-ray irradiation, thereby reducing scintillation light output and increasing afterglow.

The distribution of Al and Sc ions at garnet lattice sites was investigated using ^{27}Al and ^{45}Sc MAS NMR spectroscopy. These nuclei are particularly well-suited for NMR studies because they have 100% natural abundance and relatively large magnetic moments. The ^{27}Al and ^{45}Sc nuclei possess nuclear spins of 5/2 and 7/2, respectively, and corresponding quadrupole moments of $Q = 14.66\,fm^2$ for ^{27}Al and $-22\,fm^2$ for ^{45}Sc.

Owing to their large quadrupole moments, the shape of the ^{27}Al and ^{45}Sc NMR spectra is influenced by both chemical shift anisotropy (CSA), described by the chemical shift Hamiltonian H_{CS}, and by the interaction of the nuclear quadrupole moment with the local electric field gradient (EFG), described by the quadrupole Hamiltonian H_Q. In their principal axis systems, these Hamiltonians can be expressed as

$$H_Q = \frac{C_Q h}{4I(2I-1)}\left[3I_Z^2 - I^2 + \frac{\eta_Q}{2}(I_+ + I_-)\right], \quad \text{and}$$

$$H_{CS} = \gamma\hbar B_0 I_Z\left(\delta_{iso} + \frac{\delta_{CSA}}{2}[(2\cos^2\theta - 1) + \eta\sin^2\theta\cos 2\varphi]\right), \tag{1}$$

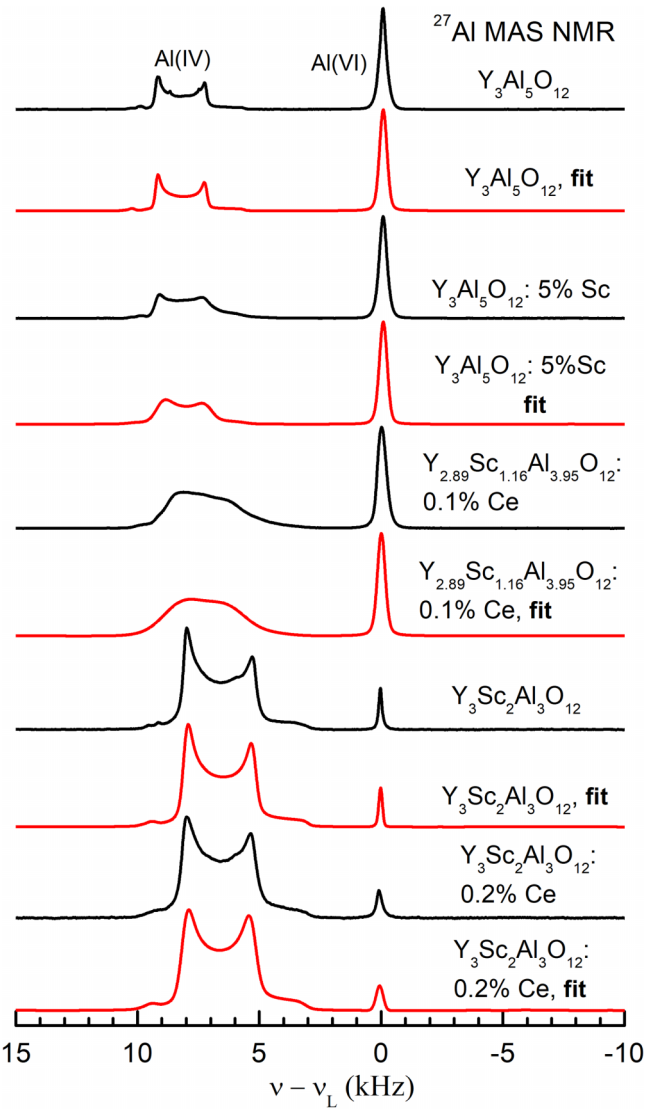

FIG. 1. ^{27}Al MAS NMR spectra of powdered $Y_3Sc_xAl_{5-x}O_{12}$ crystals recorded at a spinning rate of 24 kHz, along with the corresponding fitting curves. Only the central regions of the spectra are shown.

where $C_Q = eQV_{zz}/h$ is the quadrupole coupling constant, and V_{zz} is the largest eigenvalue of the EFG tensor. The angles θ and φ are the polar and azimuthal angles of the external magnetic field with respect to the principal x, y, and z axes of the EFG tensor. Here, δ_{iso} and δ_{CSA} denote the isotropic and anisotropic components of the chemical shift, and η is the asymmetry parameter of the chemical shift tensor [44,45]. It is commonly assumed that the principal axes of the EFG and chemical shift tensors coincide.

The central regions of the ^{27}Al MAS NMR spectra for $Y_3Sc_xAl_{5-x}O_{12}$ powder samples with varying Sc concentrations, recorded at room temperature, are shown in Fig. 1. The complete spectra, including quadrupolar spinning sidebands, are provided in Fig. S1 in the Supplemental Material [46].

The ^{27}Al MAS NMR spectra of all studied samples exhibit two main components at approximately 0 and 75 ppm, corresponding to the central transition $(1/2 \leftrightarrow -1/2)$ of aluminum

TABLE I. ^{27}Al NMR parameters for $Y_3Sc_xAl_{5-x}O_{12}$ solid solutions. Isotropic (δ_{iso}) and anisotropic (δ_{CSA}) chemical shifts are given in ppm, and the quadrupole coupling constant (C_Q) is given in kHz.

	^{27}Al(VI)					^{27}Al(IV)					
Crystal	δ_{iso}	C_Q	η_Q	δ_{CSA}	η	δ_{iso}	C_Q	η_Q	δ_{CSA}	η	Al(VI):Al(IV)
$Y_3Al_5O_{12}$	−0.5 ± 0.1	640 ± 5	0	0	0	75 ± 0.5	6050 ± 50	0	75 ± 10	0.2 ± 0.1	0.4:0.6
$Y_3Al_5O_{12}$:5% Sc	−0.5 ± 0.1	640 ± 10	0	0	0	74 ± 0.5	6060 ± 100	∼0.1	0	0	0.38:0.62
$Y_{2.89}Sc_{1.16}Al_{3.95}O_{12}$:0.1% Ce	∼0	370 ± 20	0	0	0	72 ± 2	6820 ± 300	∼0.1	90 ± 20	0.1 ± 0.1	0.16:0.84
$Y_3Sc_2Al_3O_{12}$	0.3 ± 0.1	390 ± 10	0	0	0	68 ± 0.5	7140 ± 100	∼0.1	0	0	0.02:0.98
$Y_3Sc_2Al_3O_{12}$: 0.2% Ce	0.3 ± 0.1	400 ± 10	0	0	0	68 ± 0.5	7120 ± 100	∼0.1	210 ± 40	1.0 ± 0.1	0.02:0.98

nuclei in octahedral {Al(VI)} and tetrahedral {Al(IV)} environments, respectively. All other features in the spectra correspond to spinning sidebands, whose intensity and shape are determined by CSA and quadrupolar interactions. The fitted spectral parameters, along with the calculated populations of octahedral and tetrahedral sites derived from these data are summarized in Table I.

The calculated NMR parameters for $Y_3Al_5O_{12}$ without Sc addition are in good agreement with previously reported values for this compound [7,50]. The ratio of aluminum in tetrahedral to octahedral environments is 3:2. The addition of a small amount of scandium does not significantly affect the overall calculated parameters; however, it causes a noticeable broadening and distortion of the line corresponding to aluminum in the tetrahedral environment, while the line associated with octahedral aluminum remains visually unchanged. This behavior indicates the presence of a distribution of quadrupolar interaction parameters for aluminum in tetrahedral sites.

Further increasing the scandium content in $Y_{2.89}Sc_{1.16}Al_{3.95}O_{12}$ leads to a decrease in the quadrupole coupling constant for aluminum in octahedral sites. This can be attributed to an expansion of the lattice caused by the larger ionic radius of scandium ions (with respect to Ref. [43]). Simultaneously, the quadrupole interaction constant of aluminum in tetrahedral sites gradually increases, indicating distortions of the surrounding oxygen tetrahedra. These distortions likely arise from nonlinear changes in lattice parameters due to aluminum preferentially occupying octahedral sites.

Partial substitution of aluminum by scandium also increases the distortion of the spectral line corresponding to Al(IV). This effect appears because the oxygen atoms forming the aluminum tetrahedra are shared with neighboring octahedra. The coexistence of two types of octahedra—one containing aluminum and the other scandium—with different volumes and oxygen displacements, generates a variety of local environments for the oxygen tetrahedra, resulting in a distribution of quadrupolar interaction parameters.

The addition of a small amount of cerium does not significantly affect the symmetry of the local aluminum environment but does lead to a noticeable increase in CSA. This increase is likely due to the angular dependence of the dipole-dipole interaction between the magnetic moments of Ce^{3+} paramagnetic ions and aluminum nuclei, which depends on the angle between the external magnetic field and the vector connecting the two ions.

Complete substitution of Al in octahedral sites in $Y_3Sc_2Al_3O_{12}$ is accompanied by a well-defined ^{27}Al NMR line corresponding to Al(IV), which is no longer affected by a distribution of quadrupolar interactions. It is noteworthy, however, that a low-intensity Al(VI) signal remains in the spectrum of this compound (see Fig. 1 and Table I), indicating that not all octahedral aluminum sites were fully replaced by scandium. This suggests that a small fraction of scandium may occupy other lattice positions or, more likely, that the Sc-to-Al ratio is not precisely 2:3.

The central regions of the ^{45}Sc MAS NMR spectra for powdered $Y_3Sc_xAl_{5-x}O_{12}$ samples with varying Sc concentrations, recorded at room temperature, are shown in Fig. 2. The complete spectra, including quadrupolar spinning sidebands, are presented in Fig. S2 in the Supplemental Material [46]. The main line, appearing at a chemical shift of approximately 140 ppm, corresponds to the central transition (½ ↔ – ½) of scandium nuclei in an octahedral environment. Its shape is influenced by both CSA and second-order quadrupolar interactions.

The central transitions of $Y_3Al_5O_{12}$:5% Sc, $Y_3Sc_2Al_3O_{12}$, and $Y_3Sc_2Al_3O_{12}$:Ce exhibit distinctive features, enabling direct calculation of the NMR parameters. The fitted curves and corresponding parameters are shown in Fig. 2 and summarized in Table II, respectively.

The quadrupole parameters calculated for the $Y_3Al_5O_{12}$:5% Sc sample are in good agreement with previously reported values for similar compounds [51]. In contrast, stoichiometric $Y_3Sc_2Al_3O_{12}$ samples with higher scandium content exhibit significantly lower C_Q values, reflecting reduced distortion of the local environment around scandium atoms and an increase in lattice volume, consistent with the larger ionic radius of Sc^{3+} compared with Al^{3+} [43]. Some discrepancies between the experimental and fitted spectra may arise from deviations of the fitted parameters from their actual values due to the large number of fitting variables.

A relative decrease in the intensity of the right shoulder of the spectra indicates a small distribution of quadrupolar interactions, likely caused by minor local disorder around scandium ions. Overall, however, the ^{45}Sc MAS NMR spectra of $Y_3Sc_2Al_3O_{12}$ demonstrate good chemical ordering between Sc and Al ions: Sc^{3+} predominantly occupies

TABLE II. ^{45}Sc NMR parameters for $Y_3Sc_xAl_{5-x}O_{12}$ solid solutions. Isotropic (δ_{iso}) and anisotropic (δ_{CSA}) chemical shifts are given in ppm, and the quadrupole coupling constant (C_Q) is given in kHz.

Crystal	δ_{iso}	δ_{CSA}	η	C_Q	η
$Y_3Al_5O_{12}$ 5% Sc	137 ± 3	0	0	9600 ± 400	0
$Y_{2.89}Sc_{1.16}Al_{3.95}O_{12}$	140 ± 10	—	—	7850[a]	—
$Y_3Sc_2Al_3O_{12}$	140 ± 1	60 ± 20	∼0.1	7340 ± 150	0.2 ± 0.1
$Y_3Sc_2Al_3O_{12}$:Ce	134 ± 1	160 ± 50	∼0.15	7300 ± 150	0.1 ± 0.1

[a]Average quadrupole coupling constant over the $P(V_{zz},\ \eta)$ probability [see Eq. (2)].

octahedral sites as no additional spectral lines are observed, while Al^{3+} occupies tetrahedral positions.

The ^{45}Sc NMR spectrum of $Y_{2.89}Sc_{1.16}Al_{3.95}O_{12}$:0.1% Ce does not exhibit distinct features associated with quadrupolar interactions and displays a shape typical of chemically disordered compounds. To model this spectrum, accounting for a distribution of EFG components, the Czjzek bivariate distribution of quadrupolar parameters was employed [52]

$$P(V_{zz},\eta)=\frac{V_{zz}^4\eta}{\sqrt{2\pi}\sigma^5}\left(1-\frac{\eta^2}{9}\right)\exp\left[-\frac{V_{zz}^2\left(1+\frac{\eta^2}{3}\right)}{2\sigma^2}\right], \quad (2)$$

where σ is a single adjustable parameter, which represents the width of the Gaussian distribution of the EFG components, and $P(V_{zz},\eta)$ is the joint probability of the (V_{zz},η) pair used in Eq. (2). This model is suitable for describing disordered compounds, where deviations of atoms from their equilibrium positions as well as the random distribution of aluminum and scandium atoms in the lattice lead to a Gaussian distribution of the EFG tensor components with zero mean. This corresponds to a statistically isotropic solid.

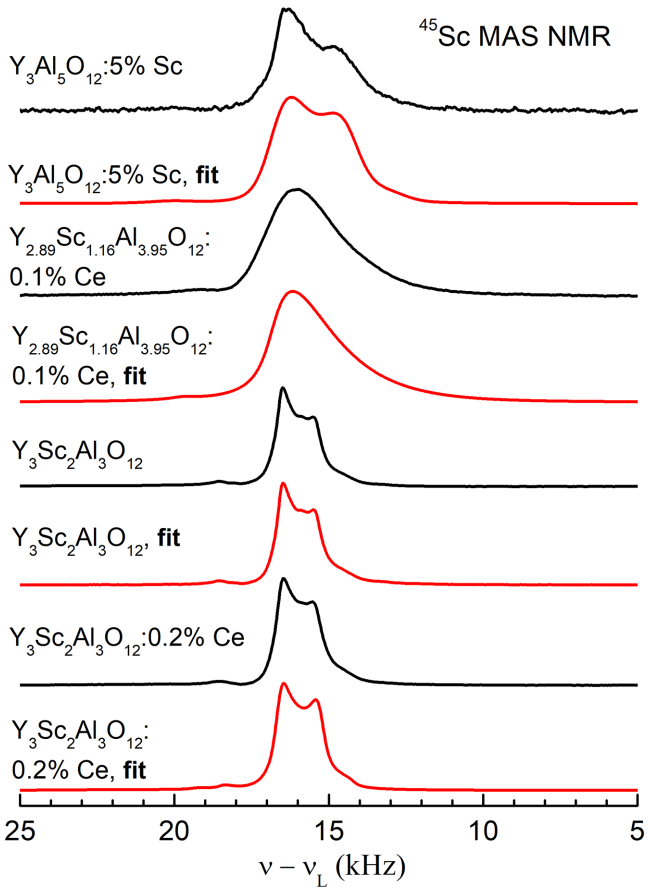

FIG. 2. ^{45}Sc MAS NMR spectra of $Y_3Sc_xAl_{5-x}O_{12}$ powders recorded at a spinning rate of 24 kHz, along with the corresponding fitting curves.

Fitting the experimental ^{45}Sc NMR line using the parameter distribution described by Eq. (2) yields an average quadrupole coupling constant of $C_Q = 7.85$ MHz. This value reflects the decreasing distortion of the oxygen octahedra surrounding scandium atoms as the degree of aluminum substitution by scandium increases.

The ^{45}Sc NMR spectrum of $Y_3Sc_2Al_3O_{12}$ exhibits a well-defined line shape, similar to that observed in ^{27}Al NMR, further confirming the high degree of chemical ordering between Sc and Al ions: Sc^{3+} predominantly occupies octahedral sites, while Al^{3+} mainly occupies tetrahedral positions.

In general, all ^{45}Sc MAS NMR spectra can be represented by a single line corresponding to scandium in octahedral environments. Although Al^{3+} in tetrahedral positions has a quadrupole coupling constant an order of magnitude larger than in octahedral positions, the corresponding quadrupole constant for Sc^{3+} in tetrahedral sites would be around 70 MHz. Such a large value would cause strong broadening of the Sc(IV) spectral line, rendering it effectively undetectable in the spectrum. Furthermore, due to the large ionic radius of Sc^{3+}, its occupancy of tetrahedral sites is highly improbable.

It should be noted that possible occupancy of Y sites by Sc ions was not detected in the ^{45}Sc NMR spectra. The spectral line of Sc^{3+} in a dodecahedral (Y) oxygen environment is expected at a lower frequency than that of Sc in octahedral coordination, according to the empirical relationship between chemical shift and oxygen coordination number [53]. This relationship is well supported by numerous experimental studies, including ^{27}Al NMR in aluminum garnets. The systematic decrease in chemical shift with increasing oxygen coordination, resulting from enhanced magnetic shielding, can be described approximately by a linear trend. A similar behavior is observed for ^{27}Al, ^{29}Si, ^{23}Na, ^{25}Mg, ^{6}Li, and ^{71}Ga [53] and is generally attributed to increased bond lengths and ionicity with higher coordination numbers.

No additional spectral lines are observed in our ^{45}Sc NMR spectra, apart from the line corresponding to Sc^{3+} in octahedral sites, indicating that the concentration of Sc ions at Y sites is below ∼0.2 at.%. This detection limit is determined by the signal-to-noise ratio of the spectra ($\sim 10^{-3}$). Corresponding zoomed-in spectra are provided in Fig. S3 in the Supplemental Material [46].

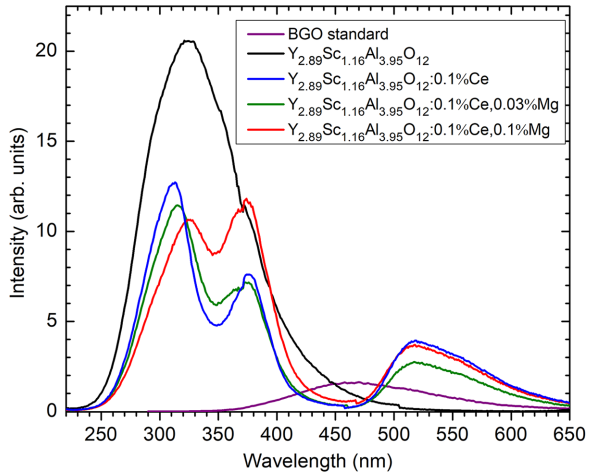

FIG. 3. RL of the set of $Y_{2.89}Sc_{1.16}Al_{3.95}O_{12}$ undoped (black line), 0.1% Ce (blue line), 0.1% Ce and 0.03% Mg (green line), and 0.1% Ce and 0.1% Mg (red line) doped crystals in absolute comparison with a BGO standard (purple line).

In contrast, EPR spectroscopy, being highly sensitive to Sc-related paramagnetic centers, can detect such antisite Sc ions at much lower concentrations than NMR. Our EPR study [33] revealed the presence of paramagnetic Sc^{2+} ions, which however are located near oxygen vacancies, which significantly enhance the probability of electron trapping at these positively charged defects (see also the Supplemental Material [46]).

B. Optical and luminescence characteristics of $Y_3Sc_xAl_{5-x}O_{12}$ crystals

Figure 3 shows the RL spectra of $Y_{2.89}Sc_{1.16}Al_{3.95}O_{12}$ crystals that are undoped, 0.1% Ce doped, and 0.1% Ce and 0.1% Mg codoped, compared in absolute intensity with a BGO standard. The undoped $Y_{2.89}Sc_{1.16}Al_{3.95}O_{12}$ crystal (black curve) exhibits a very intense luminescence peak at 324 nm, with an integrated intensity approximately 10 times higher than BGO (area under the curve: 2.15×10^7 vs 2.40×10^6 for BGO).

Doping with Ce^{3+} introduces the characteristic $5d^1 \rightarrow 4f$ emission at 518 nm and reduces the intensity of the 324 nm band. This reduction is due to the overlap with the $4f \rightarrow 5d^2$ absorption transition of Ce^{3+} at 350 nm and leads to a decrease in overall scintillation efficiency (see Table III). The addition of Mg^{2+} codopant does not produce a monotonic change in band intensities. Notably, at the highest Mg concentration, the 324 nm band shifts to longer wavelengths, suggesting a perturbation of its emission center, which is most likely an exciton localized around an Sc ion [54,55].

Upon Sc doping, the intensity of this peak decreases and shifts to longer wavelengths, indicating that some excitons are stabilized by Sc. At room temperature, this band becomes dominant even at a Sc concentration of 5%, similar to that in $Y_{2.89}Sc_{1.16}Al_{3.95}O_{12}$.

The absorption spectra of $Y_{2.89}Sc_{1.16}Al_{3.95}O_{12}$ crystals are shown in Fig. 4. The undoped crystal exhibits an absorption edge around 200 nm, while Ce^{3+}-doped samples display characteristic $4f \rightarrow 5d^1$ and $4f \rightarrow 5d^2$ transitions at 445 and 345 nm, respectively. With increasing Mg^{2+} concentration, the intensity of the Ce^{3+} absorption bands decreases, and a gradual increase in absorption below ~350 nm appears, corresponding to the Ce^{4+} charge-transfer absorption. This confirms the partial conversion of Ce^{3+} to Ce^{4+} induced by Mg^{2+} codoping. These observations are corroborated by Ce^{3+} EPR measurements, which directly show a decrease in Ce^{3+} concentration upon Mg^{2+} codoping (see Fig. S4 in the Supplemental Material [46]).

In Fig. 5, the scintillation decay of undoped $Y_{2.89}Sc_{1.16}Al_{3.95}O_{12}$ crystals is slow, with a mean decay time exceeding 800 ns. Doping with Ce significantly accelerates the decay, and this effect is further enhanced by Mg^{2+} codoping (Fig. 5 and Table III). This acceleration is attributed to the formation of stable Ce^{4+} centers, which introduce an additional fast radiative de-excitation pathway that competes with electron traps.

Despite the faster scintillation response, Ce doping leads to a decrease in light yield compared with the undoped crystal. The total scintillation efficiency, as measured by RL yield, fluctuates slightly with Mg^{2+} codoping around the value observed for the Ce-doped material. This behavior suggests that

TABLE III. Scintillation efficiency of $Y_3Sc_xAl_{1-x}O_{12}$ crystals: RL yield, LY, and scintillation mean decay time compared with BGO and GAGG:Ce. The errors of the RL/LY and the mean decay time values are within 5% and 2%, respectively.

Compound	RL yield (%)	LY (%), ^{137}Cs, 1 μs	LY (ph/MeV) ^{137}Cs, 1 μs	Mean decay time (ns)
BGO	100	100 [a]	8000	300
$Y_{2.89}Sc_{1.16}Al_{3.95}O_{12}$	900	41	3280	863
$Y_{2.89}Sc_{1.16}Al_{3.95}O_{12}$:0.1% Ce	590	19	1520	262
$Y_{2.89}Sc_{1.16}Al_{3.95}O_{12}$:0.1% Ce, 0.3% Mg	530	14	1120	344
$Y_{2.89}Sc_{1.16}Al_{3.95}O_{12}$:0.1% Ce, 0.1% Mg	660	12	960	184
$Y_3Sc_2Al_3O_{12}$ undoped 13.12.2023-c.4	900	—	—	—
$Y_3Sc_2Al_3O_{12}$-Ce 0.2%-31.1.2024-c.3 annealed 1200 °C/12 h air	160	77	6160	85
$Y_3Sc_2Al_3O_{12}$-Ce 0.2%-31.1.2024-c.5 annealed 1200 °C/12 h air	260	84	6720	111
$Gd_3Ga_{2.7}Al_{2.3}O_{12}$:0.3% Ce	—	540	42 760 [b]	147 [b]

[a]Typical absolute LY of reference BGO is 8000 ph/MeV under 662 keV excitation of ^{137}Cs.
[b]LY and mean decay time were taken from Ref. [33].

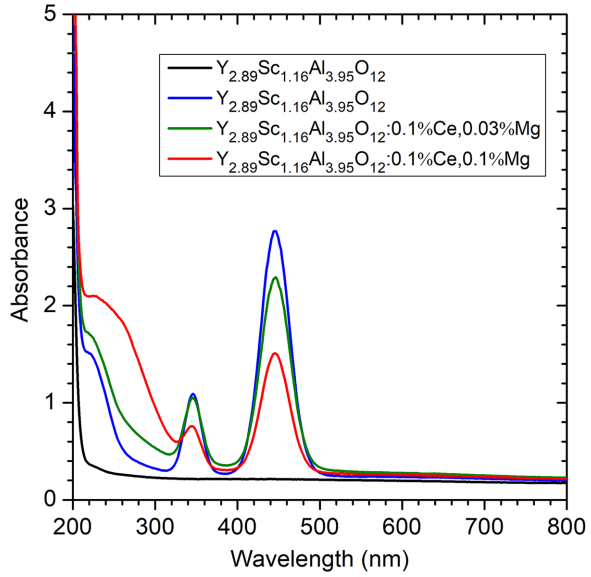

FIG. 4. Absorption spectra of the set of $Y_{2.89}Sc_{1.16}Al_{3.95}O_{12}$ undoped, 0.1% Ce, 0.1% Ce and 0.03% Mg, and 0.1% Ce and 0.1% Mg (red line) doped crystals.

Ce^{3+} introduces spatial separation of charge carriers—holes localize at Ce^{3+} ions, while electrons tend to localize near Sc ions—reducing the probability of radiative recombination and thereby decreasing the overall scintillation intensity.

In another set of crystals, the starting host composition was set to $Y_3Sc_2Al_3O_{12}$, which is closer to the congruent composition of these garnets grown from the melt, as established for the isostructural Gd-based garnet $Gd_{2.88}Sc_{1.89}Al_{3.23}O_{12}$ [31]. The undoped crystal exhibits an emission band peaking around 300 nm, similar to that shown in Fig. 3 (see Fig. 6), and its overall scintillation intensity (RL spectrum area) is comparable with that of undoped $Y_{2.89}Sc_{1.16}Al_{3.95}O_{12}$ (Table III).

Doping with Ce again produces a double-peaked UV spectrum due to overlap with the $4f-5d^2$ Ce^{3+} absorption band and reduces the RL yield which represents the overall scintillation efficiency (Fig. 6 and Table III). However, the Ce^{3+} emission dominates in the spectrum, light yield is several times higher than in $Y_{2.89}Sc_{1.16}Al_{3.95}O_{12}$:0.1% Ce, and the scintillation response is significantly faster (Table III). These observations indicate a much lower contribution from slow components on the microsecond and longer time scales, which is further supported by afterglow measurements: Following x-ray cutoff, the emission intensity decreases faster in $Y_3Sc_2Al_3O_{12}$:0.2% Ce compared with $Y_{2.89}Sc_{1.16}Al_{3.95}O_{12}$:0.1% Ce (Fig. 7). It is worth noting, however, that the afterglow of these two Sc-admixed crystals is noticeably higher compared with BGO standard sample which evidences very slow components in scintillation response due to the charge trapping and is the reason of their relatively low light yield.

For the $Y_3Sc_2Al_3O_{12}$ crystals, TSL glow curves were measured, and RL spectra were recorded before (77 K) and after (room temperature) the TSL run (Fig. 8). Interestingly, a noticeable increase in emission intensity at room temperature is observed in all cases, corresponding to the TSL glow curves. This behavior can be explained as follows. At 77 K, x-ray

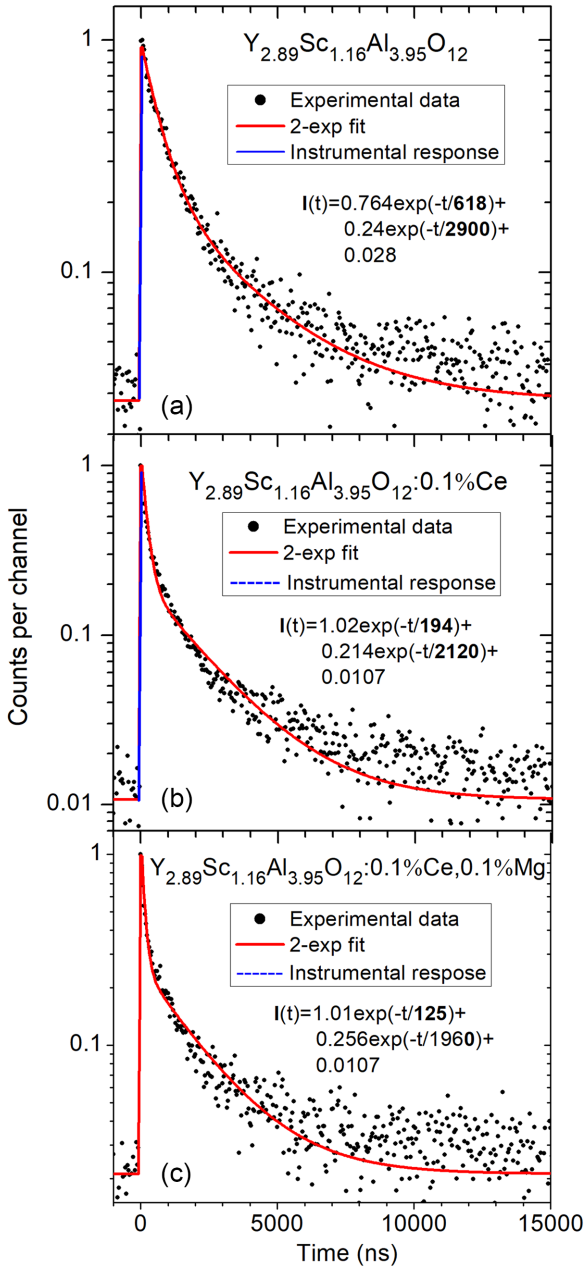

FIG. 5. Spectrally unresolved scintillation decays of (a) $Y_{2.89}Sc_{1.16}Al_{3.95}O_{12}$, (b) $Y_{2.89}Sc_{1.16}Al_{3.95}O_{12}$:0.1% Ce, and (c) $Y_{2.89}Sc_{1.16}Al_{3.95}O_{12}$:0.1% Ce and 0.1% Mg crystals. 1/e decay time values are in the figure in red.

irradiation generates charge carriers in the valence and conduction bands, but these carriers become trapped at spatially separated defect sites, strongly limiting radiative recombination. At room temperature, most of these trapped carriers are released, substantially increasing the probability of their radiative recombination.

These traps are primarily associated with host oxygen ions, which capture holes and become observable in EPR as O^- centers ($S = 1/2$, $2p^5$) (see the corresponding spectra in Figs. S5 and S6 in the Supplemental Material [46]). The O^- EPR signal is unusually intense in Sc-containing YAG crystals, indicating that these centers are formed in the

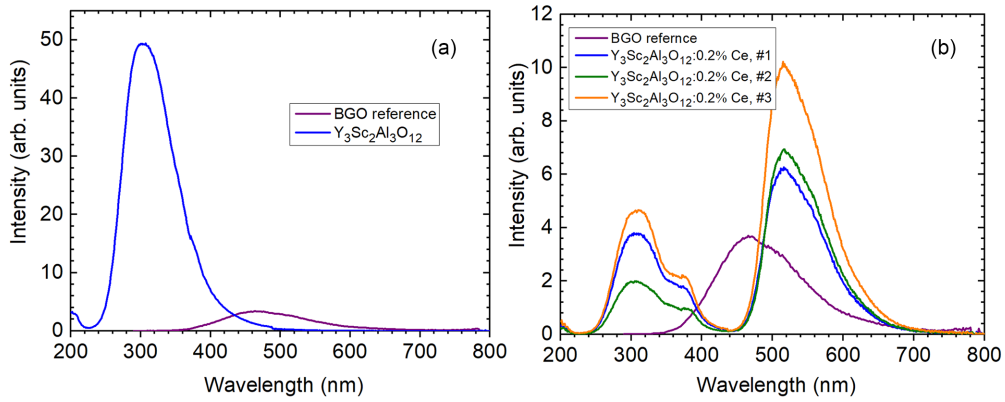

FIG. 6. Room-temperature RL spectrum of the (a) undoped and (b) Ce-doped $Y_3Sc_2Al_3O_{12}$ crystal (three different parts of the mPD grown rod) compared with that of BGO standard.

vicinity of Sc ions—most likely Sc ions occupying antisite positions. In such cases, the hole is trapped by a lattice oxygen ion near the Sc antisite, where the strong local perturbation induced by the Sc ion enhances the thermal stability of the O^- center. Note that, in Ce-doped crystal, TSL has much lower intensity as holes can also by trapped by Ce^{3+} ions forming stable Ce^{4+} centers.

Electrons are typically captured by oxygen vacancies, forming F-type centers. In Sc-doped YAG, these centers are predominantly generated near antisite Sc ions, leading to the formation of Sc^{2+}–V_O complexes [33], where the trapped electron primarily occupies the Sc $3d^1$ orbital. This interpretation is supported by the observed hyperfine interaction ($55 \times 10^{-4}\,cm^{-1}$) between the electron spin and the ^{45}Sc nuclear spin, which is close to values reported for Sc^{2+} dopants in BaF2 and SrF2 [56]. As confirmed by our DFT simulations in Sec. III C and previously for GSAG in Ref. [33], Sc antisite ions at Y lattice sites can serve as efficient electron traps.

C. Electronic band structure calculations

The electronic structure calculations and the structural optimizations were based on DFT and were performed in MedeA software by the implemented program VASP [41,42]. Calculations were based on the structure of $Y_3Al_5O_{12}$ (YAG) from the ICSD database [48]. Scandium was assumed to only enter the octahedral and dodecahedral sites. Hence, the octahedral and dodecahedral sites were occupied with Sc for 0, 1/2, 1 and 0, 1/6, 1/3 rates, respectively, creating thus nine structures with all combinations. In cases where different Wyckoff positions could be substituted, we performed structural optimizations of multiple structures and then used only the configuration with the lowest total energy.

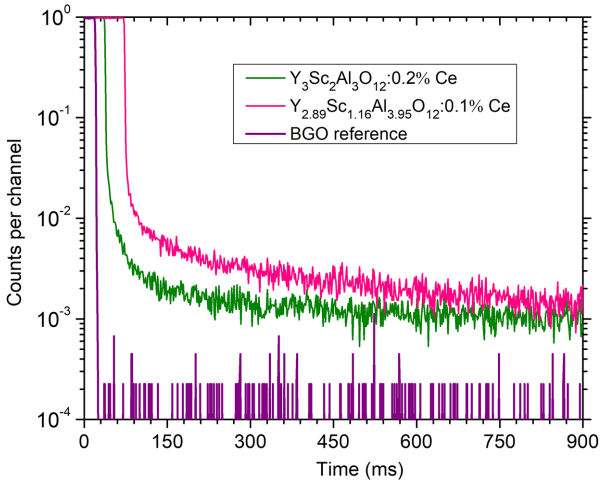

FIG. 7. Afterglow of the air annealed $Y_3Sc_2Al_3O_{12}$:0.2% Ce and $Y_{2.89}Sc_{1.16}Al_{3.95}O_{12}$:0.1% Ce crystals compared with that of BGO standard.

Structural optimizations of each of the nine structures were performed by minimizing the total energy using the conjugate gradient method, so that all atoms were relaxed and lattice parameters were allowed to change, but *Pcca* symmetry was retained. The convergence was 0.03 eV/Å. The convergence criterion was typically met after about 15 ionic steps. The lattice parameters ($a = b = c$) of the optimized structures are shown in Table S1 in the Supplemental Material [46]. The table shows a trend of increasing a with substitution of larger atoms into smaller sites (Sc in the octahedral site) and decreasing a with substitution of smaller atoms into larger sites (Sc in the dodecahedral site), which is in accordance with Vegard's law.

For the calculation of the total energies, DFT with projector augmented waves [41], general gradient approximations [57], and specific pseudopotentials Sc_sv, Y_sv, Al, and O was applied. In the self-consistent field method we used the tetrahedron method with Blöchl corrections as the integration scheme over the first Brillouin zone with the k-points spacing 0.25 $Å^{-3}$. This should be sufficient due to the large size of the cell. The same mesh with the simple tetrahedron method was used for the density of states (DOS) calculations.

In Fig. 9, the DOS and partial DOS (PDOS) are displayed for the energy region around the band gap. PDOS is shown as a sum over all Wyckoff positions occupied by a given atom weighted by the site multiplicity. The PDOS of the Sc-3d in the dodecahedral position shows a general trend of states located below the conduction band minimum, in contrast with Sc-3d in the octahedral position, which is at a level similar to some of the Y-4d states. However, the Y-4d states are likely to be energetically higher and less delocalized in reality than shown, due to the general difficulty in correctly treating the unoccupied electronic states by DFT, which could be partially

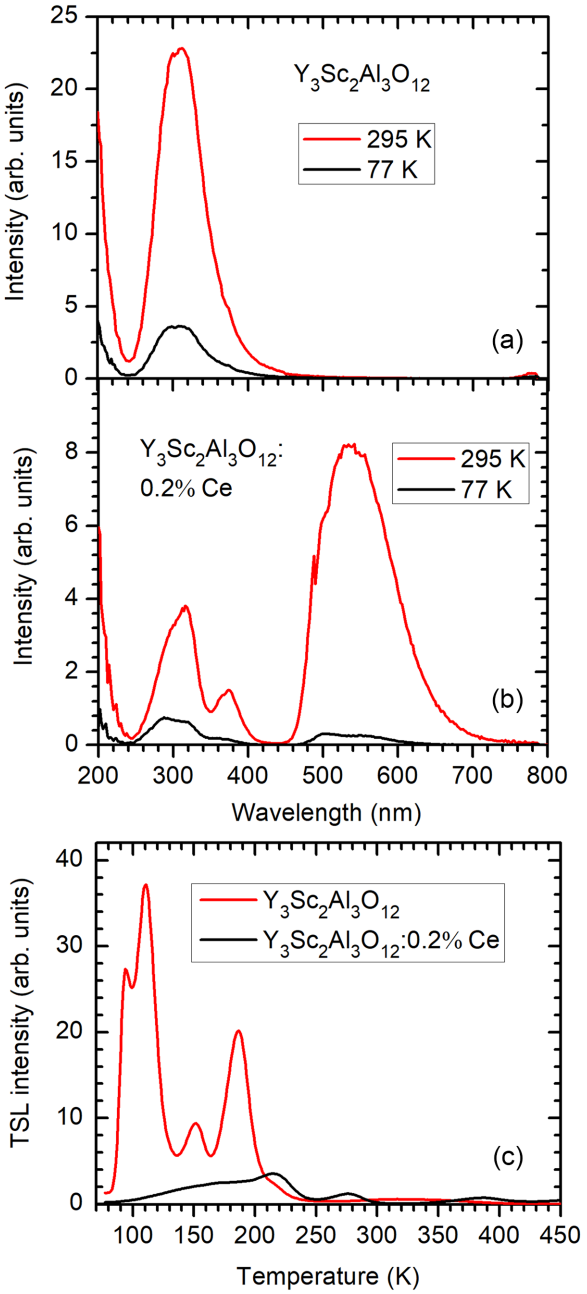

FIG. 8. (a) and (b) RL spectra of $Y_3Sc_2Al_3O_{12}$ and $Y_3Sc_2Al_3O_{12}$ 0.2% Ce crystals measured at 295 and 77 K. (c) TSL glow curves of $Y_3Sc_2Al_3O_{12}$ and $Y_3Sc_2Al_3O_{12}$ 0.2% Ce crystals x-ray irradiated at 77 K.

solved using a time-dependent method [58]. Nevertheless, in all cases, the weighted average with respect to DOS is higher for the Y-4*d* band than for the Sc-3d band.

Calculated enthalpies of formation (from oxides) of the structures are stated in the Supplemental Material [46]. While comparing the enthalpies (Table S2 in the Supplemental Material [46]), the most stable composition is $Y_3Al_5O_{12}$, with increases of enthalpy while substituting in both dodecahedral and octahedral sites, with a much steeper increase in the dodecahedral one. However, for an actual comparison of the thermodynamic stability in these crystals with high melting points, it would be necessary to evaluate the entropy of formation for receiving the free energy of formation. Thus, it is very likely that the configurational entropic term contributes to partial substitution in both sites.

IV. CONCLUSIONS

The site occupancies of Sc^{3+} and Al^{3+} ions in pure and Ce-doped $Y_3Sc_xAl_{5-x}O_{12}$ crystals were investigated using high-resolution ^{45}Sc and ^{27}Al MAS NMR spectroscopy. The NMR spectra were analyzed using a spin Hamiltonian that included magnetic Zeeman, chemical shift, and quadrupole interactions of the nuclear spins. The corresponding spin-Hamiltonian parameters were determined for Sc concentrations $x = 0$, 0.05, 1.16, and 2.

The ^{27}Al MAS NMR spectra show that Al occupies both the octahedral and tetrahedral sites of the garnet lattice. With increasing Sc concentration, the Al population at octahedral sites decreases and approaches zero for the stoichiometric $Y_3Sc_2Al_3O_{12}$ composition, indicating an almost complete replacement of Al by Sc at these sites. This observation is consistent with the ^{45}Sc NMR spectra, which exhibit only a single resonance corresponding to Sc ions at octahedral positions. The possible concentration of Sc ions occupying antisite Y dodecahedral sites was estimated to be below approximately 0.2 at.%. Such Sc ions can create a deep electron trap which is suggested by DFT calculation of electronic band structure of the Sc-admixed $Y_3Al_5O_{12}$ garnet structures.

The scintillation characteristics of pure and Ce-doped $Y_3Sc_xAl_{5-x}O_{12}$ crystals were investigated using RL, absorption, and TSL spectra as well as measurements of scintillation decay and afterglow in the nanosecond to millisecond range. The results show that the incorporation of Sc into $Y_3Al_5O_{12}$ induces a strong Sc-related exciton emission at 320–324 nm, which is nearly 10 times more intense than that in a reference BGO crystal. This emission remains pronounced even at a low Sc concentration of 5 at.%.

Doping with Ce introduces Ce^{3+} emission ($5d^1 \rightarrow 4f$ transition) at 518 nm and simultaneously reduces the intensity of the 324 nm band due to the overlap with the $4f \rightarrow 5d^2$ absorption transition of Ce^{3+} at 350 nm and leads to a decrease in overall scintillation efficiency. The scintillation decay of undoped $Y_3Sc_xAl_{5-x}O_{12}$ is relatively slow, with a mean decay time exceeding 800 ns. Doping with Ce significantly accelerates the decay, and codoping with Mg^{2+} further enhances this effect by promoting the formation of stable Ce^{4+} ions, which create an additional fast radiative de-excitation pathway that competes with electron traps. This $Ce^{3+} \rightarrow Ce^{4+}$ conversion is clearly supported by EPR spectra of Ce^{3+} in the presence of Mg^{2+} codoping.

Measurements of scintillation light yield show that, in the $Y_3Sc_2Al_3O_{12}$:Ce stoichiometric composition, it reaches a maximum of 80–84% relative to BGO, with a notably fast scintillation response characterized by a mean decay time of 85–110 ns.

Electron and hole defects, which can temporarily trap charge carriers under irradiation and thereby reduce the timing performance of scintillation, were investigated using TSL and EPR spectroscopy. It was found that holes are predominantly localized at oxygen lattice ions near Sc ions, forming O^-

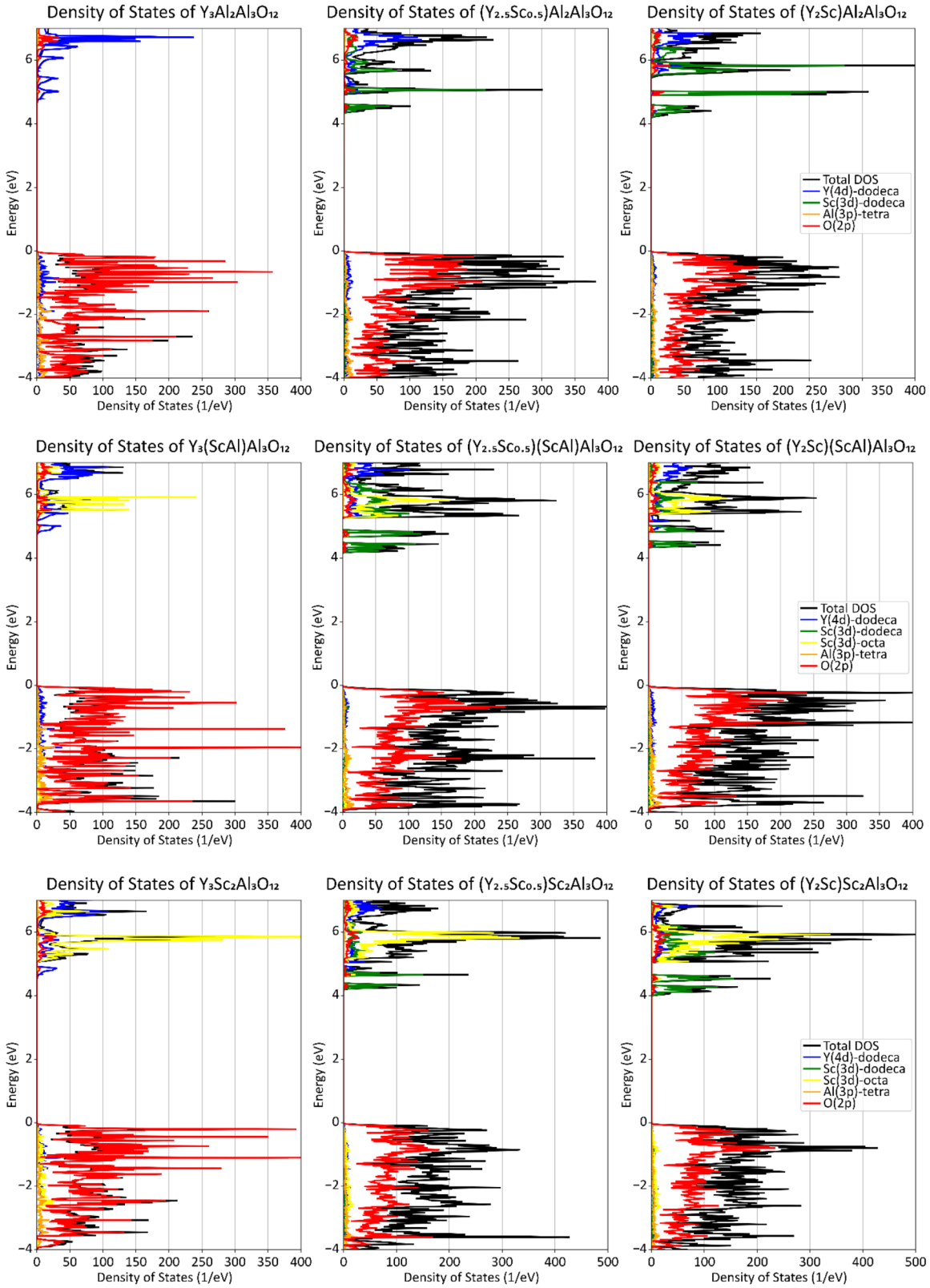

FIG. 9. The DOS and PDOS of Sc-doped $Y_3Al_5O_{12}$ structures in the energy region around the band gap. The concentration of Sc in the dodecahedral site increases in the right direction and concentration of Sc in the octahedral site increases in the downward direction.

centers whose thermal stability correlates with the observed TSL peaks. These centers are therefore active participant in the TSL processes and compete with hole trapping at Ce^{3+} luminescence ions.

Electrons generated under irradiation are suggested to be mainly trapped by Sc-antisite ions near oxygen vacancies. This is supported by the detection of Sc^{2+}–V_O centers in EPR spectra of $Y_3Sc_xAl_{5-x}O_{12}$ crystals, which exhibit a high concentration of oxygen vacancies (the crystals appear dark green). In contrast, in transparent crystals with low oxygen vacancy concentrations, Sc^{2+}–V_O centers are not detectable by EPR. Suppressing these centers by optimizing the composition (stoichiometric material appears to be most effective) and reducing oxygen vacancies contamination would significantly improve the scintillation performance of $Y_3Sc_2Al_3O_{12}$:Ce crystals. A general strategy for further optimization is therefore to limit electron localization, i.e., to engineer the bottom of the conduction band. A slight overstoichiometry of Y may also be beneficial, in analogy with GSAG:Ce (Ref. [33]).

Due to the similarity between $Y_3Sc_xAl_{5-x}O_{12}$ and $Gd_3Sc_xAl_{5-x}O_{12}$ compounds, our results on Sc-to-Al distribution in $Y_3Sc_xAl_{5-x}O_{12}$:Ce can also provide useful insights for GAGG:Ce materials.

ACKNOWLEDGMENTS

This research was supported by Czech Science Foundation Project No. 24–14580L and by OP JAC financed by ESIF and MEYS (Project No. LASCIMAT–CZ.02.01.01/00/23_-020/0008525). A.R. acknowledges the research program P1-0125 from the Slovenian Research and Innovation Agency.

DATA AVAILABILITY

The data that support the findings of this article are openly available [59], embargo periods may apply.

[1] K. Kamada, T. Endo, K. Tsutumi, T. Yanagida, Y. Fujimoto, A. Fukabori, A. Yoshikawa, J. Pejchal, and Martin Nikl, Composition engineering in cerium-doped $(Lu, Gd)_3(Ga, Al)_5O_{12}$ single-crystal scintillators, Cryst. Growth Des. **11**, 4484 (2011).

[2] K. Kamada, T. Yanagida, T. Endo, K. Tsutumi, Y. Usuki, M. Nikl, Y. Fujimoto, A. Fukabori, and A. Yoshikawa, 2inch diameter single crystal growth and scintillation properties of Ce:$Gd_3Al_2Ga_3O_{12}$, J. Cryst. Growth **352**, 88 (2012).

[3] O. Sidletskiy, V. Kononets, K. Lebbou, S. Neicheva, O. Voloshina, V. Bondar, V. Baumer, K. Belikov, A. Gektin, and B. Grinyov, Structure and scintillation yield of Ce-doped Al–Ga substituted yttrium garnet, Mater. Res. Bull. **47**, 3249 (2012).

[4] P. Dorenbos, Electronic structure and optical properties of the lanthanide activated $RE_3(Al_{1-x}Ga_x)_5O_{12}$ (RE = Gd, Y, Lu) garnet compounds, J. Lumin. **134**, 310 (2013).

[5] J. M. Ogiegło, A. Katelnikovas, A. Zych, T. Justel, A. Meijerink, and C. R. Ronda, Luminescence and luminescence quenching in $Gd_3(Ga, Al)_5O_{12}$ scintillators doped with Ce^{3+}, J. Phys. Chem. A **117**, 2479 (2013).

[6] K. Brylew, W. Drozdowski, A. J. Wojtowicz, K. Kamada, and A. Yoshikawa, Studies of low temperature thermoluminescence of GAGG:Ce and LuAG:Pr scintillator crystals using the $T_{max} - T_{stop}$ method, J. Lumin. **154**, 452 (2014).

[7] V. Laguta, Y. Zorenko, V. Gorbenko, A. Iskaliyeva, Y. Zagorodniy, O. Sidletskiy, P. Bilski, A. Twardak, and M. Nikl, Aluminum and gallium substitution in yttrium and lutetium aluminum–gallium garnets: Investigation by single-crystal NMR and TSL methods, J. Phys. Chem. C **120**, 24400 (2016).

[8] I. I. Vrubel, R. G. Polozkov, I. A. Shelykh, V. M. Khanin, P. A. Rodnyi, and C. R. Ronda, Bandgap engineering in yttrium–aluminum garnet with Ga doping, Cryst. Growth Des. **17**, 1863 (2017).

[9] C. Wang, D. Ding, Y. Wu, H. Li, X. Chen, J. Shi, Q. Wang, L. Ye, and G. Ren, Effect of thermal annealing on scintillation properties of Ce:$Gd_2Y_1Ga_{2.7}Al_{2.3}O_{12}$ under different atmosphere, Appl. Phys. A **123**, 384 (2017).

[10] M. Kitaura, H. Zen, K. Kamada, S. Kurosawa, S. Watanabe, A. Ohnishi, and K. Hara, Visualizing hidden electron trap levels in $Gd_3Al_2Ga_3O_{12}$:Ce crystals using a mid-infrared free-electron laser, Appl. Phys. Lett. **112**, 031112 (2018).

[11] V. Kochurikhin, K. Kamada, K. J. Kim, M. Ivanov, L. Gushchina, Y. Shoji, M. Yoshino, and A. Yoshikawa, Czochralski growth of 4-inch diameter Ce:$Gd_3Al_2Ga_3O_{12}$ single crystals for scintillator applications, J. Cryst. Growth **531**, 125384 (2020).

[12] M. Li, M. Meng, J. Chen, Y. Sun, G. Cheng, L. Chen, S. Zhao, B. Wan, H. Feng, G. Ren, *et al.*, Abnormal site preference of Al and Ga in $Gd_3Al_{2.3}Ga_{2.7}O_{12}$:Ce crystals, Phys. Status Solidi (B) **258**, 2000603 (2021).

[13] S. Nargelas, Y. Talochka, A. Vaitkevičius, G. Dosovitskiy, O. Buzanov, A. Vasil'ev, T. Malinauskas, M. Korzhik, and G. Tamulaitis, Influence of matrix composition and its fluctuations on excitation relaxation and emission spectrum of Ce ions in $(Gd_xY_{1-x})_3Al_2Ga_3O_{12}$:Ce scintillators, J. Lumin. **242**, 118590 (2022).

[14] D. Spassky, F. Fedyunin, E. Rubtsova, N. Tarabrina, V. Morozov, P. Dzhevakov, K. Chernenko, N. Kozlova, E. Zabelina, V. Kasimova, *et al.*, Structural, optical and luminescent properties of undoped $Gd_3Al_xGa_{5-x}O_{12}$ (x = 0,1,2,3) and $Gd_2YAl_2Ga_3O_{12}$ single crystals, Opt. Mater. **125**, 112079 (2022).

[15] A. Yoshikawa, V. V. Kochurikhin, M. Yoshino, R. Murakami, T. Tomida, I. Takahashi, K. Kamada, Y. Shoji, H. Sato, R. Kucerkova, *et al.*, Bulk single-crystal growth of Ce/$Gd_3(Al, Ga)_5O_{12}$ from melt without a precious metal crucible by pulling from a cold container, Cryst. Growth Des. **23**, 2048 (2023).

[16] T. Wu, L. Wang, Y. Shi, Q. Zhang, Y. Xiong, Q. Yuan, T. Li, K. Ma, H. Wang, J. Fang, *et al.*, A homogeneity study on $(Ce, Gd)_3Ga_2Al_3O_{12}$ crystal scintillators grown by an optical floating zone method and a traveling solvent floating zone method, CrystEngComm. **25**, 3755 (2023).

[17] Y. Wu, F. Meng, Q. Li, M. Koschan, and C. L. Melcher, Role of Ce^{4+} in the scintillation mechanism of codoped $Gd_3Ga_3Al_2O_{12}$: Ce, Phys. Rev. Appl. **2**, 044009 (2014).

[18] M. Nikl, K. Kamada, V. Babin, J. Pejchal, K. Pilarova, E. Mihokova, A. Beitlerova, K. Bartosiewicz, S. Kurosawa, and A.

Yoshikawa, Defect engineering in Ce-doped aluminum garnet single crystal scintillators, Cryst. Growth Des. **14**, 4827 (2014).

[19] S. Blahuta, A. Bessiere, B. Viana, P. Dorenbos, and V. Ouspenski, Evidence and consequences of Ce^{4+} in LYSO:Ce,Ca and LYSO:Ce,Mg single crystals for medical imaging applications, IEEE Trans. Nucl. Sci. **60**, 3134 (2013).

[20] M. T. Lucchini, V. Babin, P. Boháček, S. Gundacker, K. Kamada, M. Nikl, A. Petrosyan, A. Yoshikawa, and E. Auffray, Effect of Mg^{2+} ions co-doping on timing performance and radiation tolerance of cerium doped $Gd_3Al_2Ga_3O_{12}$ crystals, Nucl. Instr. Meth. Phys. Res. A **816**, 176 (2016).

[21] G. Tamulatis, G. Dosovitskiy, A. Gola, M. Korjik, A. Mazzi, S. Nargelas, P. Sokolov, and A. Vaitkevičius, Improvement of response time in GAGG:Ce scintillation crystals by magnesium codoping, J. Appl. Phys. **124**, 215907 (2018).

[22] G. Dantelle, G. Boulon, Y. Guyot, D. Testemale, M. Guzik, S. Kurosawa, K. Kamada, and A. Yoshikawa, Research on efficient fast scintillators: Evidence and x-ray absorption near edge spectroscopy characterization of Ce^{4+} in Ce^{3+}, Mg^{2+}-co-doped $Gd_3Al_2Ga_3O_{12}$ garnet crystal, Phys. Status Solidi B **257**, 1900510 (2020).

[23] K. Bartosiewitz, A. Markovskyi, T. Horiai, D. Szymański, S. Kurosawa, A. Yamaji, A. Yoshikawa, and Y. Zorenko, A study of Mg^{2+} ions effect on atoms segregation, defects formation, luminescence and scintillation properties in Ce^{3+} doped $Gd_3Al_2Ga_3O_{12}$ single crystals, J. Alloys Compd. **905**, 164154 (2022).

[24] L. Martinazzoli, S. Nargelas, P. Boháček, R. Calá, M. Dušek, J. Rohlíček, G. Tamulaitis, E. Auffraya, and M. Nikl, Compositional engineering of multicomponent garnet scintillators: Towards an ultra-accelerated scintillation response, Mater. Adv. **3**, 6842 (2022).

[25] S. Nargelas, A. Solovjovas, Y. Talochka, Ž. Podlipskas, M. Kucera, Z. Lucenicova, and G. Tamulaitis, Influence of heavy magnesium codoping on emission decay in Ce-doped multicomponent garnet scintillators, J. Mater. Chem. C **11**, 12007 (2023).

[26] K. Kamada, M. Nikl, T. Kotaki, H. Saito, F. Horikoshi, M. Miyazaki, K. J. Kim, R. Murakami, M. Yoshino, A. Yamaji, *et al.*, Multiple shaped-crystal growth of oxide scintillators using Mo crucible and die by the edge defined film fed growth method, J. Cryst. Growth **535**, 125510 (2020).

[27] J. Kvapil, J. Kvapil, B. Perner, R. Autrata, and P. Schauer, Czochralski growth of YAG:Ce in a reducing protective atmosphere, J. Cryst. Growth **52**, 542 (1981).

[28] D. Spassky, N. Kozlova, E. Zabelina, V. Kasimova, N. Krutyak, A. Ukhanova, V. A. Morozov, A. V. Morozov, O. Buzanov, K. Chernenko, *et al.*, Influence of the Sc cation substituent on the structural properties and energy transfer processes in GAGG:Ce crystals, CrystEngComm **22**, 2621 (2020).

[29] O. Zapadlík, J. Pejchal, R. Kučerková, A. Beitlerová, and M. Nikl, Composition-engineered GSAG garnet: Single-crystal host for fast scintillators, Cryst. Growth Des. **21**, 7139 (2021).

[30] Y.-N. Xu, W. Y. Ching, and B. K. Brickeen, Electronic structure and bonding in garnet crystals $Gd_3Sc_2Ga_3O_{12}$, $Gd_3Sc_2Al_3O_{12}$, and $Gd_3Ga_3O_{12}$ compared to $Y_3Al_3O_{12}$, Phys. Rev. B **61**, 1817 (2000).

[31] I. A. Kaurova, E. N. Domoroshchina, G. M. Kuz'micheva, and V. B. Rybakov, Evaluation of stability region for scandium-containing rare-earth garnet single crystals and their congruent-melting compositions, J. Cryst. Growth **468**, 452 (2017).

[32] L. Hovhannesyan, M. V. Derdzyan, G. Badalyan, G. Kharatyan, J. Pejchal, M. Nikl, C. Dujardin, and A. G. Petrosyan, Growth of GSAG:Ce scintillation crystals by the Bridgman method: Influence of Ce concentration and codoping, CrystEngComm. **26**, 4812 (2024).

[33] M. Nikl, J. Pejchal, J. Ježek, D. Sedmidubský, V. Laguta, V. Babin, A. Beitlerová, and R. Kučerková, GSAG:Ce scintillator: Material optimization and intrinsic bottlenecks, Mater. Adv. **6**, 3596 (2025).

[34] Y. O. Zagorodniy, V. Chlan, H. Štěpánková, Y. Fomichov, J. Pejchal, V. V. Laguta, and M. Nikl, Gallium preference for the occupation of tetrahedral sites in $Lu_3(Al_{5-x}Ga_x)O_{12}$ multicomponent garnet scintillators according to solid-state nuclear magnetic resonance and density functional theory calculations, J. Phys. Chem. Solids **126**, 93 (2019).

[35] A. Yoshikawa, M. Nikl, G. Boulon, and T. Fukuda, Challenge and study for developing of novel single crystalline optical materials using micro-pulling-down method, Opt. Mater. **30**, 6 (2007).

[36] A. Yoshikawa and V. Chani, Growth of optical crystals by the micro-pulling-down method, MRS Bull. **34**, 266 (2009).

[37] A. Fukabori, V. Chani, K. Kamada, and A. Yoshikawa, Growth of Yb-doped Y_2O_3, Sc_2O_3, and Lu_2O_3 single crystals by the micro-pulling-down technique and their optical and scintillation characterization, J. Cryst. Growth **352**, 124 (2012).

[38] O. Zapadlík, J. Pejchal, F. Levchenko, R. Kučerková, A. Beitlerová, V. Vaněček, K. Jurek, and M. Nikl, The Ga-admixed GSAG:Ce single crystal scintillator: Composition tuning, J. Lumin. **263**, 119984 (2023).

[39] TopSpin software for both routine and advanced NMR acquisition and analysis, https://www.bruker.com/en/products-and-solutions/mr/nmr-software/topspin.html.

[40] D. Massiot, F. Fayon, M. Capron, I. King, S. Le Calvé, B. Alonso, J. -O. Durand, B. Bujoli, Z. Gan, and G. Hoatson, Modelling one- and two-dimensional solid-state NMR spectra, Magn. Res. Chem. **40**, 70 (2002).

[41] G. Kresse and J. Furthmüller, Efficient iterative schemes for *ab initio* total-energy calculations using a plane-wave basis set, Phys. Rev. B **54**, 11169 (1996).

[42] G. Kresse and J. Furthmüller, Efficiency of *ab-initio* total energy calculations for metals and semiconductors using a plane-wave basis set, Comput. Mater. Sci. **6**, 15 (1996).

[43] R. D. Shannon, Revised effective ionic radii and systematic studies of interatomic distances in halides and chalcogenides, Acta Cryst. A **32**, 751 (1976).

[44] A. Abragam, *Principles of Nuclear Magnetism* (Oxford University Press, New York, 1961).

[45] J. F. Bangher, P. C. Taylor, T. Oja, and P. J. Bray, Nuclear magnetic resonance powder patterns in the presence of completely asymmetric quadrupole and chemical shift effects: Application to metavanadates, J. Chem. Phys. **50**, 4914 (1969).

[46] See Supplemental Material at http://link.aps.org/supplemental/10.1103/png3-xnt7 for the high-resolution ^{27}Al and ^{45}Sc MAS NMR spectra of $Y_3Sc_xAl_{5-x}O_{12}$, Ce^{3+} EPR data, EPR of x-ray irradiation induced centers, and details of electronic band structure calculations, which includes Refs. [33,41,42,47–49].

[47] H. R. Lewis, Paramagnetic resonance of Ce^{3+} in yttrium aluminum garnet, J. Appl. Phys. **37**, 739 (1966).

[48] F. Euler and J. A. Bruce, Oxygen coordinates of compounds with garnet structure, Acta Cryst. **19**, 971 (1965).

[49] A. D. Becke, Perspective: Fifty years of density-functional theory in chemical physics, J. Chem. Phys. **140**, 18A301 (2014).

[50] Th. Vosegaard, I. P. Byriel, D. A. Pawlak, K. Wozniak, and H. J. Jakobsen, Crystal structure studies on the garnet $Y_3Al_5O_{12}$ by ^{27}Al single-crystal NMR spectroscopy, J. Am. Chem. Soc. **120**, 7900 (1998); N. Gautier, D. Massiot, I. Farnan, and J. P. Coutures, Aluminium-gallium substitution in yttrium garnets investigated by NMR, J. Chim. Phys. **92**, 1843 (1995).

[51] C. Tien, E. V. Charnaya, S. Y. Sun, R. R. Wu, S. N. Ivanov, and E. N. Khazanov, ^{27}Al and ^{45}Sc NMR studies of the $Y_3Sc_xAl_{5-x}O_{12}$ mixed garnets, Phys. Status Solidi B **233**, 222 (2002).

[52] G. Czjzek, J. Fink, F. Götz, H. Schmidt, J. M. D. Coey, J.-P. Rebouillat, and A. Liénard, Atomic coordination and the distribution of electric field gradients in amorphous solids, Phys. Rev. B **23**, 2513 (1981).

[53] K. J. D. Mackenzie and M. E. Smith, *Multinuclear Solid-State NMR of Inorganic Materials*, Pergamon Materials Series Vol. 6 (Elsevier Science, Amsterdam, 2002).

[54] V. Murk and N. Yaroshevich, Exciton and recombination processes in YAG crystals, J. Phys.: Condens. Matter **7**, 5857 (1995).

[55] N. N. Ryskin, P. Dorenbos, C. W. E. van Eijk, and S. Kh. Batygov, Scintillation properties of $Lu_3Al_{5-x}Sc_xO_{12}$ crystals, J. Phys.: Condens. Mater **6**, 10423 (1994).

[56] U. T. Hochli, Jahn-Teller effect of a d^1 ion in eightfold cubic coordination, Phys. Rev. **162**, 262 (1967).

[57] J. P. Perdew, K. Burke, and M. Ernzerhof, Generalized gradient approximation made simple, Phys. Rev. Lett. **77**, 3865 (1996).

[58] K. Burke, J. Werschnik, and E. K. U. Gross, Time-dependent density functional theory: Past, present, and future, J. Chem. Phys. **123**, 062206 (2005).

[59] V. Laguta, Text and OriginLab files for figures with complete dataset [Data set], Zenodo (2026), https://doi.org/10.5281/zenodo.19475379.